Title
System Identification of a MEMS Gyroscope

Journal
Journal of Dynamic Systems Measurement and Control, 123(2)

ISSN
0022-0434

Authors
M'Closkey, Robert T
Gibson, Steve
Hui, Jason

Publication Date
2001-06-01

DOI
10.1115/1.1369360

Peer reviewed

System Identification of a MEMS Gyroscope *

Robert T. M'Closkey† Steve Gibson Jason Hui
Assistant Professor Professor Graduate Research Assistant

Mechanical and Aerospace Engineering Department
University of California
Los Angeles, CA 90095

February 2000

Abstract

This paper reports the experimental system identification of the Jet Propulsion Laboratory MEMS vibratory rate gyroscope. A primary objective is to estimate the orientation of the stiffness matrix principal axes for important sensor dynamic modes with respect to the electrode pick-offs in the sensor. An adaptive lattice filter is initially used to identify a high-order two-input/two-output transfer function describing the input/output dynamics of the sensor. A three-mode model is then developed from the identified input/output model to determine the axes' orientation. The identified model, which is extracted from only two seconds of input/output data, also yields the frequency split between the sensor's modes that are exploited in detecting the rotation rate. The principal axes' orientation and frequency split give direct insight into the source of quadrature measurement error that corrupts detection of the sensor's angular rate.

1 Introduction

A new generation of microelectromechanical (MEMS) gyroscope is being developed at the Jet Propulsion Laboratory for spacecraft applications such as attitude stabilization, maneuver control, and tumble recovery. The advantages of this system over conventional inertial navigation instruments include: compact size and weight savings, low power consumption, and a low cost micro-machining process. Microgyroscopes will augment other external inertial reference systems such as the Global Positioning System (GPS), sun sensor, or star tracker in future planetary fly-by and landing, and interplanetary astrophysics research programs, will use this technology. Tang et al. (1996a) gives an overview of the role of micro-inertial systems in spacecraft. The summary by Yazdi et al. (1998) describes other efforts to develop a MEMS gyroscope.

For the microgyros to realize the performance levels of which they are capable, innovative methods are required for device calibration and active control of sensor dynamics. The necessity of such methods

*This work is supported by Hughes Electronics through UC MICRO Grant No. 96113 and the California Institute of Technology Grant No. PF-433.

†Corresponding author: (310) 825-2909, rtm@obsidian.seas.ucla.edu

arises from the fact that the mechanical properties of MEMS are inherently sensitive to their operating environment; their dynamic characteristics can vary significantly with temperature and pressure. Also, because of the microscopic scale of key mechanical components, fabrication irregularities can produce a wide range of dynamic responses among any batch of supposedly identical devices. The sensitivity and variability of sensor dynamics must be compensated for by precise calibration of individual devices based on the detailed modeling and identification from input/output (I/O) data, and often by active control loops built into the sensor.

The JPL microgyroscope, like all vibratory rate sensors, relies on the dynamic coupling of elastic modes within the sensor. In these devices, a degree of freedom is driven to a constant, known amplitude and as the sensor is rotated the driven motion is coupled into a second degree of freedom via a coriolis term. The angular rate of rotation of the sensor may be inferred from the response amplitude of this second degree of freedom (often called the sense mode) and in a high sensitivity device, the amplitude of coriolis-induced motion may be several orders of magnitude smaller than the response of the driven degree of freedom. This poses a challenging sensing task since the electronic pick-offs usually observe all elastic modes of the sensor.

Each vibratory rate sensor design addresses this issue in a unique way. Zhbanov and Zhuravlev (1998), for example, show how the hemispherical resonator gyro uses mass balancing of the vibrating structure to modify its modal properties into producing a more favorable response. Tuning fork rate gyros, and error sources in these devices, are discussed in Newton (1963) and Morrow (1955). A comprehensive error analysis of a simplified vibratory gyro model is presented by Lynch (1995,1998) where he addresses both force rebalance and open-loop operation.

The JPL microgyro in its most ideal configuration blends measurements of two pick-offs to make the driven motion unobservable thereby sensing only the coriolis-induced response. The pick-off signals are usually combined in a sum and difference manner even though the driven mode and coriolis-induced deflections are not isolated by the new measurements. The extent to which the driven mode corrupts the measurement of the coriolis-induced motion is essentially determined by the orientation of the principal axes of the stiffness matrix, associated with two elastic sensor modes, with respect to the electronic pick-offs.

This paper introduces a procedure to estimate the orientation of the stiffness matrix principal axes, or stiffness axes for brevity, with respect to the sensing and actuation electrodes. The method uses only I/O data from the drive electrodes to the sense pick-offs. We show that the principal axes of the prototype tested for this paper do not align themselves with the natural body-fixed axes based on the mechanical symmetry of the sensor. Furthermore, the process of packaging the microgyro in a hermetically sealed high-vacuum enclosure can introduce stresses that modify its modal properties. In a packaged device, however, it is impossible to employ optical instruments that can make direct measurements of the axes' orientation so our approach is especially useful when optical access is limited. The strongest motivation for determining the stiffness axes' orientation, however, comes from the fact that the orientation may be "tuned", much like the frequency split between the modes is reduced with electronic tuning, to improve sensor performance.

Our two-step approach to estimate the axes' orientation first applies modern system identification (ID)

algorithms to identify multivariable I/O models of the JPL microgyro. These high-order models capture the dynamics of the sensor's mechanical structure as well as those of the sensing and actuation electrodes. The I/O models of the gyro reveal important sensor properties such as modal frequencies and damping ratios and are also suitable for control loop design as described in M'Closkey et al. (1999). At the second step, we obtain a reduced-order model of the primary gyro dynamics that is based on the identified high-order model and demonstrate how, under certain assumptions, the orientation of the stiffness matrix principal axes can be determined from this model.

Our approach has the advantage of yielding tractable computational problems at each step. For example, the identification of the I/O model is achieved using a numerically stable lattice filter that fits an ARX model to the I/O data. A high-order model only takes several seconds to compute from 20,000 points (two seconds) of multichannel data. The rigid body model is derived from the high-order model after an appropriate truncation and its salient features are extracted using simple singular value decompositions of the reduced order state-space data. An alternative method is to compute the rigid body model parameters in one step by optimizing the fit of this model to the I/O data. The difficulty with this approach, however, is that the model parameters enter into the computations in an essentially nonlinear fashion that requires global optimization to solve.

The paper is organized as follows: Section 2.1 describes the physical aspects of the JPL microgyro, Section 2.2 discusses the rate measurement error sources, Section 3.1 briefly discusses the ARX model structure used in the identification of a high-order sensor model, and Section 3.2 proposes a method for computing the orientation of the stiffness matrix principal axes. The experimental results are compiled in Section 4. The identification results are presented in Section 4.1, and an estimate of the orientation of the stiffness axes is pursued in Section 4.2. Our justification of treating the gyro dynamics as if they were governed by classically damped second order equations is given is Section 5.1, and supporting elaboration on the response of the sensor's modes is made in Section 5.2. The analysis is Section 5 is postponed until after the identification results are reported in Section 4 because the identified frequencies and damping ratios are required for the numerical studies discussed in Section 5. Section 6 concludes the paper.

2 Vibratory Rate Gyro Principles

2.1 The JPL Microgyroscope

Excitation of the JPL microgyro dynamics is achieved by applying a potential to the two drive electrodes, denoted D_1 and D_2, in Figure 1. The drive electrodes, and sensing pick-offs labeled as S_1 and S_2 in this figure, are suspended by silicon springs above matching electrodes on the base plate. The large central post is rigidly attached to the "cloverleaf" formed by D_1, D_2, S_1 and S_2. The post adds inertia to the system which boosts the sensitivity to rotational motion. The electrical potential between the drive electrodes and their respective base-plate electrodes creates an electrostatic force that pulls the electrodes towards each other and this applied torque causes the cloverleaf assembly to tilt or rock. The displacement of the cloverleaf structure causes a rate-of-change of capacitance between the sensing electrodes and their

respective base-plate electrodes. These signals are measured with transimpedance amplifiers and provide estimates of the velocity at two points on the cloverleaf assembly. Further information on the operating principles of the microgyro, fabrication details, and preliminary performance results may be found in Tang et al. (1996b,1997). A description of other non-MEMS vibratory gyro technologies is covered in Lawrence (1998).

The rocking of the cloverleaf assembly is actually the response of two modes of the elastically suspended structure. An appreciable response amplitude can only be achieved when driving the system near these modal frequencies. These modes have equal frequencies and no damping in an ideal device and, in this degenerate situation, any line through the origin of the x–y axes in Figure 1 represents an axis about which the post can be made to rock. A natural choice for the driven mode in this case is to make the cloverleaf rock periodically about the y-axis in Figure 1. This *drive rocking mode* is excited by applying the same periodic potential to D_1 and D_2 as this creates a torque about the y axis. If the device is rotated with angular rate Ω about the z-axis, then the periodic y-axis response is coupled into the x-axis degree of freedom via coriolis acceleration. The response about the x-axis is referred to as the *sense rocking mode* and its motion is related to Ω. The sense rocking mode response is simply measured by taking the difference between the S_1 and S_2 pick-off measurements. Similarly, the drive rocking mode response is measured by summing S_1 and S_2 and is used as a feedback signal when exciting this degree of freedom.

Actual microgyros, however, do not have equal sense and drive rocking mode frequencies nor can they be made with zero damping. This implies that the x and y-axes may not be modal axes associated with the cloverleaf rocking modes. Thus, the detection of the coriolis-induced deflections using the sensing scheme noted above is now subject to various errors. Similarly, setting D_1 equal to D_2 no longer excites just one rocking mode in this case. The next section presents the linearized model of the JPL microgyroscope and identifies signals which corrupt the angular rate measurement in any practical device.

2.2 Gyro Analytical Model and Rate Measurement Error Sources

The gyroscopic dynamics of the JPL sensor can be captured by modeling the cloverleaf as a thin, uniform, rigid plate with a uniform post, or cylinder, mounted perpendicular to the plate at its center. The plate has moment of inertia I_0 and the post has moment of inertia I_p about in-plane principal axes through the center of the plate. The plate and post under go small out-of-plane rotations ψ_x and ψ_y about gyro-fixed x and y axes in Figure 2, and the gyro rotates at the rate Ω about its z-axis. The plate is attached elastically to the gyro housing, and control torques τ_x and τ_y are applied to the plate about the x and y axes, respectively. The linearized equations of motion for this model are

$$\begin{bmatrix} I_0+I_p & 0 \\ 0 & I_0+I_p \end{bmatrix} \begin{bmatrix} \ddot{\psi}_x \\ \ddot{\psi}_y \end{bmatrix} + 2\Omega \begin{bmatrix} 0 & -I_p \\ I_p & 0 \end{bmatrix} \begin{bmatrix} \dot{\psi}_x \\ \dot{\psi}_y \end{bmatrix} + \underbrace{\begin{bmatrix} \hat{c}_{11} & \hat{c}_{12} \\ \hat{c}_{12} & \hat{c}_{22} \end{bmatrix}}_{C} \begin{bmatrix} \dot{\psi}_x \\ \dot{\psi}_y \end{bmatrix} + \underbrace{\begin{bmatrix} k_{11} & k_{12} \\ k_{12} & k_{22} \end{bmatrix}}_{K} \begin{bmatrix} \psi_x \\ \psi_y \end{bmatrix} = \begin{bmatrix} \tau_x \\ \tau_y \end{bmatrix}. \quad (1)$$

The stiffness matrix K is positive definite, and the damping matrix C is at least positive semidefinite. These equations reveal that the vertical post is responsible for the coriolis coupling between the two

rocking modes.

The linearized equations of motion for all vibratory gyroscopes possess the same canonical structure (see Lynch (1995,1998), for example). However, the parameterization in (1) in terms of I_0 and I_p is unique to the JPL design, and the skew-symmetric matrix reveals the way in which the JPL device achieves the coriolis coupling between the two vibration modes.

The JPL microgyro, as in most vibratory rate sensors, operates in a *force rebalance* mode. In this case, the y-axis is designated as the drive axis and is excited by τ_y into a harmonic oscillation with stable amplitude and frequency. The objective of the force rebalance scheme is to drive ψ_x to zero by appropriate specification of τ_x. In the ideal rate sensor with identical modal frequencies and no dissipation, τ_x is proportional to Ω (see (4) below). In the non-ideal sensor the principal axes of K and C are not aligned with each other nor with the x and y axes. The excitation and control of ψ_y and ψ_x are carried out with feedback loops as shown in Figure 3. The upper loop is designed to produce $\dot{\psi}_y = A\cos(\omega_0 t + \phi_0)$ and the lower loop regulates ψ_x to zero. The angular rate Ω is treated as an external disturbance and the next paragraphs demonstrate how Ω can be detected from the sense rebalance torque τ_x.

The ψ_x and ψ_x coordinates are not very transparent for revealing terms in the sensor dynamics that govern the sensor's performance. A more convenient coordinate system is defined in which K is diagonal,

$$\begin{bmatrix}\psi_1\\ \psi_2\end{bmatrix} = \underbrace{\begin{bmatrix}\cos\theta & \sin\theta\\ -\sin\theta & \cos\theta\end{bmatrix}}_{\mathcal{O}} \begin{bmatrix}\psi_x\\ \psi_y\end{bmatrix},$$

where ψ_1 and ψ_2 are small rotations of the cloverleaf plate about the new gyro-fixed x_1 and x_2 axes that coincide with the stiffness matrix principle axes, and $\mathcal{O}$ is the real orthonormal matrix that diagonalizes K, i.e.,

$$\mathcal{O}K\mathcal{O}^T = \begin{bmatrix}\hat{k}_1 & 0\\ 0 & \hat{k}_2\end{bmatrix}.$$

Figure 2 shows the relation of both coordinate systems as well as other parameters that will be used in Section 3.2. The eigenvalues of K, or principal stiffnesses, are denoted $\hat{k}_1$ and $\hat{k}_2$. Rewriting (1) in terms of the new coordinates yields

$$\begin{bmatrix}\ddot{\psi}_1\\ \ddot{\psi}_2\end{bmatrix} + 2\Omega\frac{I_p}{I_{0,p}}\begin{bmatrix}0 & -1\\ 1 & 0\end{bmatrix}\begin{bmatrix}\dot{\psi}_1\\ \dot{\psi}_2\end{bmatrix} + \begin{bmatrix}c_{11} & c_{12}\\ c_{12} & c_{22}\end{bmatrix}\begin{bmatrix}\dot{\psi}_1\\ \dot{\psi}_2\end{bmatrix} + \begin{bmatrix}\omega_1^2 & 0\\ 0 & \omega_2^2\end{bmatrix}\begin{bmatrix}\psi_1\\ \psi_2\end{bmatrix} = \frac{1}{I_{0,p}}\begin{bmatrix}\sin\theta\\ \cos\theta\end{bmatrix}\tau_y + \frac{1}{I_{0,p}}\begin{bmatrix}\cos\theta\\ -\sin\theta\end{bmatrix}\tau_x, \quad (2)$$

where $\omega_i^2 = \hat{k}_i/(I_0 + I_p)$, $i = 1, 2$, $I_{0,p} = I_0 + I_p$, and

$$\begin{bmatrix}c_{11} & c_{12}\\ c_{12} & c_{22}\end{bmatrix} = \frac{1}{I_{0,p}}\mathcal{O}C\mathcal{O}^T.$$

In this coordinate system, parameters such as modal frequencies and off-diagonal damping terms are defined and will be used in the error analysis.

Our objective in this section is to derive the equations for ψ_y– the drive axis dynamics– and the ideal sense-axis torque, denoted τ_{rb}, that enforces the constraint $\psi_x(t) \equiv 0$ for all t (the rebalance force). Note that $\psi_y = \psi_1 \sin\theta + \psi_2 \cos\theta$ by definition and $\psi_1 \cos\theta = \psi_2 \sin\theta$ from the rebalance requirement. The following expressions are developed using these relations:

$$\ddot{\psi}_y + \left(c_{11}\sin^2\theta + c_{22}\cos^2\theta + c_{12}\sin 2\theta\right)\dot{\psi}_y + \left(\omega_1^2\sin^2\theta + \omega_2^2\cos^2\theta\right)\psi_y = \tau_y \tag{3}$$

$$\tau_{rb} = \frac{1}{2}\left(\omega_1^2 - \omega_2^2\right)(\sin 2\theta)\,\psi_y + \left(\frac{1}{2}(c_{11}-c_{22})\sin 2\theta + \frac{1}{2}c_{12}\cos 2\theta - 2\frac{I_p}{I_{0,p}}\Omega\right)\dot{\psi}_y. \tag{4}$$

The largest possible sinusoidal response amplitude of ψ_y is desired since this scales the torque rebalance signal (see (5)). A drive axis control loop to achieve this objective, shown in Figure 3, may be designed using (3). The torque required to keep ψ_x at zero is displayed in (4) and is denoted τ_{rb} (the subscript indicates "rebalance"). This torque may be closely approximated by the control signal generated from a high-gain feedback loop closed from τ_x to ψ_x, also shown in Figure 3. We will assume for purposes of the error analysis that $\dot{\psi}_y(t) = A\cos\omega_0 t$, for some fixed response amplitude, A, and frequency ω_0 (the phase may be taken to be zero without loss of generality), so that the rebalance torque is written as

$$\tau_{rb} = A\left(\underbrace{\frac{1}{2}\frac{\omega_1^2-\omega_2^2}{w_0}\sin 2\theta\sin\omega_0 t}_{\text{source of quadradure error}} + \underbrace{\frac{1}{2}\Big((c_{11}-c_{22})\sin 2\theta + c_{12}\cos 2\theta\Big)\cos\omega_0 t}_{\text{source of in-phase error}} - \underbrace{2\frac{I_p}{I_{0,p}}\Omega\cos\omega_0 t}_{\text{desired term}}\right). \tag{5}$$

The terms in (5) give much insight into error sources that produce measurement biases and corrupt the estimate of Ω. The sources may be grouped into *in-phase* and *quadrature* terms as labeled in (5). Rotation of the sensor with angular rate Ω produces a rebalance torque proportional to $\Omega\cos\omega_0 t$. Damping in the sensor, however, also produces a torque that is in-phase with, and hence indistinguishable from, the one produced by Ω.

Another significant error source is the *quadrature* term in (5). This error is present because of frequency mismatch between the rocking modes, i.e., $\omega_1 \neq \omega_2$, in addition to misalignment between the stiffness axes and the pick-offs that measure $\dot{\psi}_y$ and $\dot{\psi}_x$, i.e, $\theta \neq 0$. Note that ω_0 is usually selected as either ω_1 or ω_2, so in this case $(\omega_1^2 - \omega_2^2)/\omega_0 \approx 2(\omega_1 - \omega_2)$. The quadrature error may be significantly reduced by using phase sensitive detection in which τ_{rb} is demodulated with respect to a *measurement* of $\dot{\psi}_y$. More specifically, when $\dot{\psi}_y$ is measured, a small phase error is incurred and the demodulating signal becomes $A\cos(\omega_0 t + \phi_E)$, where ϕ_E is the measurement's phase error. Demodulating τ_{rb} by multiplication with $A\cos(\omega_0 t + \phi_E)$ and then filtering to remove the high frequency harmonics, produces the following estimate of the sensor rotation rate

$$\frac{A}{2}\left(-\frac{1}{2}\frac{\omega_1^2-\omega_2^2}{w_0}\sin 2\theta\sin\phi_E + \frac{1}{2}\Big((c_{11}-c_{22})\sin 2\theta + c_{12}\cos 2\theta\Big)\cos\phi_E - 2\frac{I_p}{I_{0,p}}\Omega\cos\phi_E\right). \tag{6}$$

The in-phase error is minimized by constructing sensors with as little damping as possible, that is, reducing the magnitude of c_{ij}. The quadrature error for many designs becomes the limiting factor in the ability to

recover Ω. As is evident from (6), the quadrature error is essentially proportional to the product of three terms: 1) the frequency split, $\omega_1 - \omega_2$, 2) misalignment of the principal axes of elasticity with the sensing pick-offs, θ, and 3) the demodulation phase error, ϕ_E.

A common practice is to close the rebalance and drive control loops in vibratory rate sensors when $\Omega = 0$ and directly determine the quadrature and in-phase bias errors to within the confidence specified by the demodulation phase error. The individual contributions to these biases, however, cannot be resolved using this method. Thus, direct measurement of θ provides more insight into the bias errors and may assist in tuning the gyro dynamics to improve performance.

3 Identification Methods

3.1 ARX Input/Output Models

The two-mode model (1) is useful for explaining the basis of the JPL microgyro operation but in reality the sensor has more complex dynamics. There is another significant degree of freedom that results in plunging of the post and leaves along the z-axis in Figure 1. Furthermore, there is some electrical cross-coupling between the drive electrodes and pick-offs. A higher-order I/O model is necessary to capture these features.

The first step of the system identification fits an input/output model to experimental data. This data fit is done in the time domain. The objective is to accurately model the dynamic response of the gyroscope, when $\Omega = 0$, as represented by the two-input/two-output transfer function from drives D_1 and D_2 to pick-offs S_1 and S_2. This transfer function is assumed to have the form of the linear ARX (Auto-Regressive with eXogenous input) model

$$A(q^{-1})\vec{y} = B(q^{-1})\vec{u}, \tag{7}$$

where A and B are 2×2 matrix polynomials in the delay operator q^{-1}, and $\vec{y}$ and $\vec{u}$ represent the 2×1 measured output sequences and applied input sequences, respectively.

Accurate identification of the two rocking modes is necessary for estimating θ and the frequency split. The raw data includes linear vibration modes and their harmonics. The harmonics are primarily due to nonlinear distortion introduced by the capacitive sensing scheme. For system identification, we use a bandpass filter to remove most of the higher-harmonic content from the output sequences before identifying a transfer function. However, even after this procedure, there remains signal power from higher frequency modes and harmonics, and this residual power outside of the bandwidth of interest is sufficient to require the use of high-order models for accurate identification of the rocking modes. Furthermore, there is a prominent *up-down mode* whose frequency is close to the rocking mode frequencies. The bandpass filtering does not remove the up-down mode from the data and hence this mode is identified along with the rocking modes.

The adaptive multichannel lattice filter algorithm developed in Jiang and Gibson (1995) is used to identify high order models. This algorithm fits the model in (7) to the input/output data using a least-squares

criterion. The features that make the lattice filter attractive for microsystem applications are its suitability for real-time implementation, numerical efficiency and stability at high orders, and rapid convergence of parameter estimates. Furthermore, identification of other classes of complex flexible structures has shown that multiple input and output channels must be used to identify two or more modes with very close frequencies and earlier versions of the multi-channel lattice filter used here have proved effective for such tasks (see, for example, Jiang et al., 1992).

3.2 Computing Stiffness Matrix Principal Axes from Input/Output Models

A systematic and reliable method for determining the rocking mode frequency split, $\omega_1 - \omega_2$, and the angle θ between the gyro-fixed x and y axes and the stiffness axes is developed in this section and represents an improvement over measuring just the aggregate terms. This analysis is complementary to the usual tests performed on vibratory rate sensors and may be used to screen sensor prototypes, or alternatively, perform on-line tuning to drive the modal frequencies closer together and θ to zero.

We consider the situation in which the damping principal axes are the same as the stiffness axes. We will subsequently show in Section 5.1 that this is a reasonable assumption for the gyro under test. The part of the identified ARX model that represents the rocking modes in continuous-time state-space form is given by (2), without rate input Ω, and with the off-diagonal damping set to zero:

$$\begin{bmatrix} \ddot{\psi}_1 \\ \ddot{\psi}_2 \end{bmatrix} + \begin{bmatrix} c_{11} & 0 \\ 0 & c_{22} \end{bmatrix} \begin{bmatrix} \dot{\psi}_1 \\ \dot{\psi}_2 \end{bmatrix} + \begin{bmatrix} \omega_1^2 & 0 \\ 0 & \omega_2^2 \end{bmatrix} \begin{bmatrix} \psi_1 \\ \psi_2 \end{bmatrix} = \frac{1}{I_{0,p}} \begin{bmatrix} \sin\theta \\ \cos\theta \end{bmatrix} \tau_y + \frac{1}{I_{0,p}} \begin{bmatrix} \cos\theta \\ -\sin\theta \end{bmatrix} \tau_x. \tag{8}$$

This model is not complete, however, because the controlled variables in the JPL sensor are not torques about the x and y axes but rather forces applied at the D_1 and D_2 electrodes. We define two scale factors, K_{D_1} and K_{D_2}, that convert the electrical potentials on D_1 and D_2 into forces. The scale factors are allowed to be different because of possible variations in electrode area, etc. The distributed electrode forces are replaced with equivalent point forces and, due to the symmetric fabrication of the drive electrodes, the point forces are assumed to act at the center of its corresponding electrode. Thus, the point forces are converted into torques with moment arm l about the x and y axes (see Figure 2). This leads to the following relationship between the applied voltages and torques

$$\begin{bmatrix} \tau_x \\ \tau_y \end{bmatrix} = l \underbrace{\begin{bmatrix} -1 & 1 \\ 1 & 1 \end{bmatrix}}_{\mathcal{M}_D} \underbrace{\begin{bmatrix} K_{D_1} & 0 \\ 0 & K_{D_2} \end{bmatrix}}_{\mathcal{K}_D} \begin{bmatrix} D_1 \\ D_2 \end{bmatrix}. \tag{9}$$

The matrices $\mathcal{M}_D$ and $\mathcal{K}_D$ are defined as shown. Positive torques and angular velocities conform to the right-handed convention and this defines the signs of the $\mathcal{M}_D$ elements.

The sensor outputs are voltages proportional to the distributed sense electrode velocities. As in the drive electrode case, we assume that the electrode voltage is proportional to the velocity at the center of the electrode. The contributions of the angular velocity about the x and y axes with moment arm l are

combined, through the matrix $\mathcal{M}_S$, to yield the total electrode velocity. Displacements in the negative z-axis direction are considered positive. The conversion factors from velocity to voltage for each electrode are denoted K_{S_1} and K_{S_2} and are used to define the scaling matrix $\mathcal{K}_S$ as shown in (10). Thus, the gyroscope output equation is

$$\begin{aligned}\begin{bmatrix} S_1 \\ S_2 \end{bmatrix} &= l \underbrace{\begin{bmatrix} K_{S_1} & 0 \\ 0 & K_{S_2} \end{bmatrix}}_{\mathcal{K}_S} \underbrace{\begin{bmatrix} -1 & -1 \\ 1 & -1 \end{bmatrix}}_{\mathcal{M}_S} \begin{bmatrix} \dot{\psi}_x \\ \dot{\psi}_y \end{bmatrix} \\ &= l\mathcal{K}_S\mathcal{M}_S \begin{bmatrix} \cos\theta & -\sin\theta \\ \sin\theta & \cos\theta \end{bmatrix} \begin{bmatrix} \dot{\psi}_1 \\ \dot{\psi}_2 \end{bmatrix}.\end{aligned} \tag{10}$$

Combining (8), (9), and (10) into a multi-input/output transfer function yields

$$\begin{aligned}\begin{bmatrix} S_1/D_1 & S_1/D_2 \\ S_2/D_1 & S_2/D_2 \end{bmatrix} = &\frac{s}{s^2 + c_{11}s + \omega_1^2} \underbrace{\frac{l^2}{I_{0,p}} \mathcal{K}_S\mathcal{M}_S \begin{bmatrix} \cos\theta \\ \sin\theta \end{bmatrix} \begin{bmatrix} \cos\theta & \sin\theta \end{bmatrix} \mathcal{M}_D\mathcal{K}_D}_{M_1, \text{ first Markov parameter associated with mode 1}} + \\ &\frac{s}{s^2 + c_{22}s + \omega_2^2} \underbrace{\frac{l^2}{I_{0,p}} \mathcal{K}_S\mathcal{M}_S \begin{bmatrix} -\sin\theta \\ \cos\theta \end{bmatrix} \begin{bmatrix} -\sin\theta & \cos\theta \end{bmatrix} \mathcal{M}_D\mathcal{K}_D}_{M_2, \text{ first Markov parameter associated with mode 2}}.\end{aligned} \tag{11}$$

A calculation with the state space representation of (8) in which the modes are decoupled yields the expressions for the first Markov parameters (the product "CB" from the state space matrices) shown in (11). The form of this transfer function suggests a method for determining θ:

1. identify the two rocking modes in the gyroscope dynamics,
2. after a state-space transformation in which the modes are decoupled, compute the first Markov parameter for each mode, denoted M_1 for mode one and M_2 for mode two,
3. compute the matrices $\tilde{M}_i = (\mathcal{K}_S\mathcal{M}_S)^{-1} M_i (\mathcal{M}_D\mathcal{K}_D)^{-1}$, $i = 1, 2$,
4. $\tilde{M}_1$ is, ideally, rank one and its left and right singular vectors corresponding to the non-zero singular value are equal to $\begin{bmatrix} \cos\theta & \sin\theta \end{bmatrix}^T$ (alternatively, $\tilde{M}_2$ is also rank one and its singular vectors are equal to $\begin{bmatrix} -\sin\theta & \cos\theta \end{bmatrix}^T$),
5. determine θ from the singular vectors.

This method requires the $\mathcal{K}_S$ and $\mathcal{K}_D$ gain matrices. Estimates of these gains are made in Section 4.2.

4 Experimental Results

4.1 Identified Models

Chirp signals (continuously swept sinusoids), generated at a sampling rate of 10 kHz and passed though a zero-order hold, are used to excite the gyro. The D_1 input is swept linearly from 400 Hz to 700 Hz over a three-second period while the D_2 input is swept linearly from 700 Hz down to 400 Hz over three seconds. These frequency ranges were chosen after a simple test with a spectrum analyzer indicated the presence of sensor modes in this frequency range. The inputs are swept in opposite directions to ensure that they are independent sequences thereby fully exciting the gyro dynamics from each input channel. In fact, the JPL gyro, with its very closely spaced rocking modes, motivates the application of MIMO identification methods. In the degenerate case where the modes are equal, the system is not observable from a single pick-off measurement nor controllable from a single drive channel. Thus, at least two inputs and two outputs are required to properly identify the modes. The inputs have a 4-volt peak-to-peak amplitude with a 5-volt bias and they are directly applied to the electrodes from the D/A board.

The voltage measurements from the sensing pick-offs are filtered through identical analog low-pass filters (8-pole Butterworth), with 4.8 kHz corner frequencies for anti-aliasing, before being sampled at 10 kHz. The filters also provide an additional 20 dB boost to ensure that the measurements nearly span the 16-bit range of the A/D converters. Figure 4 shows the sampled output sequences for one experiment and their corresponding power spectral densities (PSD). The distinct beat frequencies evident in the outputs indicate the presence of closely spaced modes. The drive inputs are not shown since no details are visible except on short time scales.

The PSDs of the output sequences have significant energy between 500 Hz and 600 Hz (the modes we wish to model), 1000 Hz to 1200 Hz (the second harmonics due to measurement nonlinearities), and integer multiples of 60 Hz (AC hum). The signal content from the higher harmonics is removed prior to system identification by filtering both the input and output sequences with an 8^{th}-order Chebychev bandpass filter with IIR transfer function $G_{\text{bp}}(q^{-1})$. The filtered signals are denoted by $\vec{y}_{\text{bp}}$ and $\vec{u}_{\text{bp}}$; i.e.,

$$\vec{y}_{\text{bp}} = G_{\text{bp}}(q^{-1})\vec{y}, \qquad \vec{u}_{\text{bp}} = G_{\text{bp}}(q^{-1})\vec{u}. \tag{12}$$

The lower corner frequency for the bandpass filter is 400 Hz and the higher corner frequency is 700 Hz (taken to match swept frequency range). Multiplying (7) by $G_{\text{bp}}(z)$ yields

$$A(q^{-1})\vec{y}_{\text{bp}} = B(q^{-1})\vec{u}_{\text{bp}}. \tag{13}$$

This is the discrete-time two-input/two-output model used for system identification. The Chebychev filter weights the prediction error according to the window specified by G_{bp}, thereby forcing the identification algorithm to concentrate on modeling the sensor dynamics in this frequency range. The bandpass filter adds no net phase to the identified model because both the input and output sequences are filtered, i.e., $\vec{y}_{\text{bp}}$ and $\vec{u}_{\text{bp}}$ are delayed the same amount.

Models with orders ranging from 10 to 80 were identified from several data sets. It is not necessary to use three seconds of data, corresponding to the period of the sweep input, to obtain good identification results. In fact, the lattice filter processed a two-second data window (20,000 points per channel) centered on the portion of the data record that contained the largest signal output. For example, this would correspond to using the data between 0.5 seconds and 2.5 seconds in Figure 4. Using longer data sets did not improve the identified parameter estimates although a model order of 40 was usually necessary before the phase in the bandwidth of interest stopped changing significantly. The results presented here are for I/O models of order 40. Finally, because we use an unwindowed lattice filter to fit a time-domain model directly to the I/O data, non-zero initial and final conditions in the data introduce no bias in the modal parameter estimates.

Figure 5 displays the magnitude of the broad-band frequency response of the 40th-order two-input/two-output identified model. Inspection of the model reveals two modes less than 2 Hz apart near 535 Hz. These modes are the rocking modes of the elastic structure and may be clearly seen in Figure 6 (solid line) where the frequency axis has been scaled to focus on the modes. Extracting the modal frequencies from the identified model yields rocking modes at 534.5 Hz and 536.4 Hz. The third mode evident in the frequency response plots is determined from the model to be 590.3 Hz. This higher frequency mode is verified to be the up-down mode by focusing a laser vibrometer on the drive and sense cloverleaves as the gyro is driven at this frequency. The vibrometer provides a direct means of measuring the mechanical displacement of the leaves and the fact that the motion of all of the leaves are in-phase when forced at this frequency indicates that the up-down mode is being excited. The frequency of the up-down mode is independently determined to be 590.0 Hz using a precision function synthesizer and vibrometer. Confirmation of the rocking mode frequencies at 534.6 Hz and 536.5 Hz is also made with the vibrometer. Thus, the modal frequencies determined from the identified model are very close to these independent measurements. The identified model, however, provides us with a complete picture of the sensor dynamics.

The two rocking modes and up-down mode dominate the frequency response of the gyro so it is useful to consider the three mode approximation of the 40th-order model. This can be accomplished by performing a truncation of the balanced state realization of the 40th-order model. Balanced realizations and model reduction are discussed in Green and Limebeer (1995), and Zhou, Doyle, and Glover (1996). The eight largest Hankel singular values of the 40th-order model are

$$\begin{bmatrix} 15.2 & 15.2 & 6.75 & 6.75 & 3.49 & 3.48 & 0.0652 & 0.0651 \end{bmatrix}.$$

Truncating the system to the first six states of the balanced realization results in very small approximation error as is evident from these Hankel singular values. The eigenvalues of this six state system are three sets of complex conjugate pairs forming a three mode system approximating the rocking modes and up-down mode of the gyro dynamics. A sixth order model is not identified directly because there is enough signal energy in the frequency range excluding the gyro modal frequencies to bias the parameter estimates in the ARX model if only six states are used in the model. Thus, even though the gyro dynamics are well-approximated by a six state system, an accurate fit of the I/O data requires a higher model order.

The frequency responses of the four channels of the 40th-order model and six state model are compared in Figure 6. For the subsequent analysis, the discrete-time models have been mapped to the continuous-time models by inverting the zero-order hold operator because it is more intuitive to discuss modal parameters like frequency and damping ratio for continuous-time models.

The continuous-time transfer function representation for the six state model is

$$\begin{aligned}\begin{bmatrix}\tilde{S}_1/D_1 & \tilde{S}_1/D_2\\ \tilde{S}_2/D_1 & \tilde{S}_2/D_2\end{bmatrix} =& \frac{1}{d_1(s)}\left(s\begin{bmatrix}6.067 & -0.9687\\ -21.06 & 3.649\end{bmatrix}+\begin{bmatrix}7063 & -397.6\\ -54670 & 5861\end{bmatrix}\right)\\ &+\frac{1}{d_2(s)}\left(s\begin{bmatrix}-5.423 & -19.02\\ -1.233 & -4.559\end{bmatrix}+\begin{bmatrix}-5408 & -50450\\ -727.3 & -9474\end{bmatrix}\right)\\ &+\frac{1}{d_3(s)}\left(s\begin{bmatrix}21.31 & 21.34\\ 23.09 & 23.13\end{bmatrix}+\begin{bmatrix}64680 & -64740\\ 69500 & 69570\end{bmatrix}\right).\end{aligned} \tag{14}$$

This transfer function relates the drive voltage input to the pick-off voltage. The polynomials d_1, d_2 and d_3 are the two rocking modes and up-down mode dynamics, respectively, where

$$\begin{aligned}
&d_1(s) = s^2 + 2\zeta_1\omega_1 s + \omega_1^2, \quad \zeta_1 = 3.167\times10^{-4}, \quad \omega_1 = 534.5 * 2\pi \text{ rad/s} && \text{(first rocking mode)}\\
&d_2(s) = s^2 + 2\zeta_2\omega_2 s + \omega_2^2, \quad \zeta_2 = 1.586\times10^{-4}, \quad \omega_2 = 536.4 * 2\pi \text{ rad/s} && \text{(second rocking mode)}\\
&d_3(s) = s^2 + 2\zeta_3\omega_3 s + \omega_3^2, \quad \zeta_3 = 11.70\times10^{-4}, \quad \omega_3 = 590.3 * 2\pi \text{ rad/s} && \text{(up-down mode).}
\end{aligned} \tag{15}$$

The sense channels in (14) are written $\tilde{S}_i$ to remind us that the identified model includes the phase-lag introduced by the anti-aliasing filter. One would expect (14) to contain only s terms in the numerator because the sensing arrangement measures the electrode velocity relative to the base plate. The anti-aliasing filter, however, changes the phase of the measurements in the frequency range of the modes (the amplitude is not modified).

The effect of the anti-aliasing filter must be removed since Section 4.2 requires models based only on the mechanical structure of the gyro. This can be accomplished with *phase correction* by approximating each modal contribution in the transfer function (14), on a channel-by-channel basis, with the product of a transfer function based on velocity measurements, $\beta s/d_i(s)$, and the anti-aliasing filter, G_{aa}. The parameter β is chosen to minimize the error between the frequency response of (14) and $G_{\text{aa}}(s)\frac{\beta s}{d_i(s)}$. For example, the first rocking mode transfer function excluding the anti-aliasing filter for the S_1/D_1 channel is approximated as $\beta_0 s/d_1(s)$ where β_0 is determined from

$$\beta_0 := \arg\min_{\beta} \left\| \frac{6.067s + 7063}{d_1(s)} - G_{\text{aa}}(s)\frac{\beta s}{d_1(s)} \right\|_\infty, \tag{16}$$

where $\|\cdot\|_\infty$ is the $\mathcal{H}_\infty$ norm. The computation is convex in β so a simple bisection routine is used to calculate the optimum.

This approximation yields the following transfer function relating the drive inputs to the sense mea-

surements without the anti-aliasing filter dynamics

$$\begin{bmatrix} S_1/D_1 & S_1/D_2 \\ S_2/D_1 & S_2/D_2 \end{bmatrix} = \frac{s}{d_1(s)}M_1 + \frac{s}{d_2(s)}M_2 + \frac{s}{d_3(s)}M_3 \tag{17}$$

where M_1, M_2, and M_3 are the first Markov parameter matrices from the state-space data of the reduced-order and phase corrected model,

$$M_1 = \begin{bmatrix} 6.240 & -0.8787 \\ -26.52 & 4.014 \end{bmatrix}, \quad M_2 = \begin{bmatrix} -5.425 & -24.10 \\ 1.153 & -5.355 \end{bmatrix}, \quad M_3 = \begin{bmatrix} 27.49 & 27.53 \\ 29.70 & 29.74 \end{bmatrix}.$$

Thus, (17) is the closest approximation to the mechanical structure of the gyro that we are able to make assuming the primary source of phase lag in the identified model is due to the anti-aliasing filters. Factors such as electrode area and component variation in the signal conditioning circuits can produce small relative gain differences between the measurement channels. The phase lag introduced by the pick-off signal conditioning amplifiers, however, is minimal in the frequency range of the three modes.

4.2 Identified stiffness axes

Estimating θ, the orientation of the principal axes of the stiffness matrix, using the steps outlined in Section 3.2 requires knowledge of scaling matrices $\mathcal{K}_S$ and $\mathcal{K}_D$ that convert sense electrode velocity into the electrode potential, and drive electrode potential into electrode force. The up-down mode has an important role in determining this data. Measurements with the laser vibrometer have revealed that the up-down mode is essentially translational in the z axis direction in the JPL gyroscope. Thus, any discrepancy between the sense electrode measurements when this mode is excited may be attributed to an imbalance in the pick-off gains, K_{S_1} and K_{S_2}, that define the scaling matrix $\mathcal{K}_S$. Similarly, the drive electrode forces have an identical effect on the up-down mode so if the modal response differs when applying a given signal to D_1 and then to D_2, the discrepancy may be attributed to the electrode efficiency in converting the applied electrode potential to a force, i.e., the gains K_{D_1} and K_{D_2} that comprise the scaling matrix $\mathcal{K}_D$. Thus, assuming the up-down mode is purely translational allows us to write it in the transfer function form

$$\begin{aligned} &\frac{s}{d_3(s)} \begin{bmatrix} K_{S_1} & 0 \\ 0 & K_{S_2} \end{bmatrix} \begin{bmatrix} 1 \\ 1 \end{bmatrix} \begin{bmatrix} 1 & 1 \end{bmatrix} \begin{bmatrix} K_{D_1} & 0 \\ 0 & K_{D_2} \end{bmatrix} \\ &\qquad = \frac{s}{d_3(s)} \begin{bmatrix} K_{S_1} \\ K_{S_2} \end{bmatrix} \begin{bmatrix} K_{D_1} & K_{D_2} \end{bmatrix}, \end{aligned} \tag{18}$$

where $d_3(s)$ has been defined in (15). Comparing (18) to the identified model (17) shows that K_{S_1}, K_{S_2}, K_{D_1}, and K_{D_2} may be estimated to within a constant from the data matrix M_3. The SVD of M_3 is

$$M_3 = \begin{bmatrix} 0.6793 & 0.7338 \\ 0.7338 & -0.6793 \end{bmatrix} \begin{bmatrix} 57.27 & 0 \\ 0 & 1.370 \times 10^{-5} \end{bmatrix} \begin{bmatrix} 0.7066 & 0.7076 \\ 0.7076 & -0.7066 \end{bmatrix}^T.$$

The rank one approximation of M_3 is

$$57.27 \begin{bmatrix} 0.6793 \\ 0.7338 \end{bmatrix} \begin{bmatrix} 0.7066 & 0.7076 \end{bmatrix},$$

and so the sense electrode and drive electrode gains are computed to be

$$\begin{bmatrix} K_{S_1} \\ K_{S_2} \end{bmatrix} = \nu_S \begin{bmatrix} 0.6793 \\ 0.7338 \end{bmatrix} \qquad \begin{bmatrix} K_{D_1} \\ K_{D_2} \end{bmatrix} = \nu_D \begin{bmatrix} 0.7066 \\ 0.7076 \end{bmatrix}.$$

The constants ν_S and ν_D reflect the fact that we cannot uniquely determine the gains without knowing the actual velocity of the up-down mode response. Also, note that M_3 is almost rank one, as predicted by the analytical model (18), since its condition number is greater than 4×10^6. The rank condition of the data matrices also provides a quantitative check of the identified model. The singular vectors from the up-down mode data indicate a sense electrode gain imbalance of about 7.4%, and very little difference between the drive electrodes.

It is now possible to estimate θ by computing the SVDs of $\tilde{M}_i = (\mathcal{K}_S \mathcal{M}_S)^{-1} M_i (\mathcal{M}_D \mathcal{K}_D)^{-1}$, $i = 1, 2$,

$$\begin{aligned}
\tilde{M}_1 &= \begin{bmatrix} 0.8593 & 0.5114 \\ -0.5114 & 0.8593 \end{bmatrix} \begin{bmatrix} \frac{26.6797}{\nu_S \nu_D} & 0 \\ 0 & \frac{0.0656}{\nu_S \nu_D} \end{bmatrix} \begin{bmatrix} 0.8045 & -0.5940 \\ -0.5940 & -0.8045 \end{bmatrix}^T \\
&\approx \frac{26.6797}{\nu_S \nu_D} \underbrace{\begin{bmatrix} 0.8593 \\ -0.5114 \end{bmatrix}}_{\vec{u}_1} \underbrace{\begin{bmatrix} 0.8045 & -0.5940 \end{bmatrix}}_{\vec{v}_1^T} \\
\tilde{M}_2 &= \begin{bmatrix} 0.5505 & 0.8349 \\ 0.8349 & -0.5505 \end{bmatrix} \begin{bmatrix} \frac{26.2276}{\nu_S \nu_D} & 0 \\ 0 & \frac{0.0490}{\nu_S \nu_D} \end{bmatrix} \begin{bmatrix} 0.5346 & -0.8451 \\ 0.8451 & 0.5346 \end{bmatrix}^T \\
&\approx \frac{26.2276}{\nu_S \nu_D} \underbrace{\begin{bmatrix} 0.5505 \\ 0.8349 \end{bmatrix}}_{\vec{u}_2} \underbrace{\begin{bmatrix} 0.5346 & 0.8451 \end{bmatrix}}_{\vec{v}_2^T}.
\end{aligned}$$

The condition numbers of these matrices are greater than 400 and this justifies the rank one approximation required by the analysis. The singular vectors from $\tilde{M}_1$, denoted $\vec{u}_1$ and $\vec{v}_1$, are predicted to be equal from the analytical model (11). Similarly, $\vec{u}_2$ and $\vec{v}_2$, the singular vectors from $\tilde{M}_2$, should also be equal and their inner product with $\vec{u}_1$ and $\vec{v}_1$ should be zero. These conditions are approximately satisfied, however, instead of obtaining one estimate of θ by combining all of the information provided by the singular vectors, we use each vector to independently estimate θ according to $\begin{bmatrix} \cos\theta_{\vec{u}_1}, & \sin\theta_{\vec{u}_1} \end{bmatrix} = \vec{u}_1^T$, $\begin{bmatrix} \cos\theta_{\vec{v}_1}, & \sin\theta_{\vec{v}_1} \end{bmatrix} = \vec{v}_1^T$, $\begin{bmatrix} -\sin\theta_{\vec{u}_2}, & \cos\theta_{\vec{u}_2} \end{bmatrix} = \vec{u}_2^T$, and $\begin{bmatrix} -\sin\theta_{\vec{v}_2}, & \cos\theta_{\vec{v}_2} \end{bmatrix} = \vec{v}_2^T$, where $\theta_{\vec{u}_1}$, $\theta_{\vec{v}_1}$, $\theta_{\vec{u}_2}$, and $\theta_{\vec{v}_2}$ are four estimates of θ. This yields

$$\begin{bmatrix} \theta_{\vec{u}_1}, & \theta_{\vec{v}_1}, & \theta_{\vec{u}_2}, & \theta_{\vec{v}_2} \end{bmatrix} = \begin{bmatrix} -30.76, & -36.44, & -33.40, & -32.31 \end{bmatrix} \text{ degrees.}$$

The largest discrepancy between the estimates is less than 6 degrees, and the estimates using the second rocking mode differ by about 1 degree. There are many possible factors contributing to the differences between the estimates and refining this analysis is subject of ongoing research. We also employed a laser vibrometer to verify the approximate orientation of the stiffness axes by observing the nodes associated each modal response. Space limitations, however, preclude presentation of the vibrometer results.

It is informative to interpret the frequency response plots in Figure 6 in terms of the orientation of principal stiffness axes. For example, in the S_2/D_1 channel Bode plot, the magnitude of the lower frequency rocking mode at $\omega_1 = 534.5$ Hz is much larger than the magnitude of the higher frequency rocking mode at $\omega_2 = 536.4$ Hz. Furthermore, our analysis shows that the lower frequency mode responds about the axis defined by θ. This means the D_1 drive electrode has large authority in exciting this mode and that the mode is highly observable with the S_2 sense electrode. Both of these effects conspire synergistically to produce a large peak at 534.5 Hz in the S_2/D_1 channel. A similar argument may be employed to justify why the higher frequency rocking mode has very little contribution to this channel: the mode at ω_2 rocks about its axis which is 90 degrees to θ; this axis almost bisects the D_1 and S_2 electrodes and hence the mode is difficult to excite and observe with this sensor/actuator pair. It is possible to apply this reasoning to the other channels that yields interpretations that are consistent with the remaining Bode plots. Thus, this analysis also provides insight into the asymmetrical aspects of the frequency response in Figure 6 and indicates that this gyro will have significant quadrature errors even though the frequency split is less than 0.4%.

5 The Effects of a Non-Diagonal Damping Matrix

5.1 Impact of off-diagonal damping on stiffness axes estimate

Section 3.2 proposed an algorithm for estimating the stiffness axes orientation, θ, under the condition that the damping matrix is also diagonalized by the stiffness matrix eigenvectors. This assumption is not true in practice, however, we will demonstrate for the device under test that the details of the damping matrix may be neglected. First, consider the state-space representation of (2) with $\Omega = 0$,

$$\begin{aligned}
\frac{d}{dt}\begin{bmatrix}\psi_1\\ \dot\psi_1\\ \psi_2\\ \dot\psi_2\end{bmatrix} &= \underbrace{\begin{bmatrix}0 & 1 & 0 & 0\\ -\omega_1^2 & -c_{11} & 0 & -c_{12}\\ 0 & 0 & 0 & 1\\ 0 & -c_{12} & -\omega_2^2 & -c_{22}\end{bmatrix}}_{A}\begin{bmatrix}\psi_1\\ \dot\psi_1\\ \psi_2\\ \dot\psi_2\end{bmatrix} + \frac{l}{I_{0,p}}\underbrace{\begin{bmatrix}0 & 0\\ \cos\theta & \sin\theta\\ 0 & 0\\ -\sin\theta & \cos\theta\end{bmatrix}}_{B}\mathcal{M}_D\mathcal{K}_D\begin{bmatrix}D_1\\ D_2\end{bmatrix}\\
\begin{bmatrix}S_1\\ S_2\end{bmatrix} &= \mathcal{K}_S\mathcal{M}_S\underbrace{\begin{bmatrix}0 & \cos\theta & 0 & -\sin\theta\\ 0 & \sin\theta & 0 & \cos\theta\end{bmatrix}}_{C}\begin{bmatrix}\psi_1\\ \dot\psi_1\\ \psi_2\\ \dot\psi_2\end{bmatrix}.
\end{aligned} \tag{19}$$

The state-space matrices are partitioned into 2×2 sub-matrices such that

$$A = \begin{bmatrix} A_{11} & A_{12} \\ A_{21} & A_{22} \end{bmatrix}, \quad B = \begin{bmatrix} B_1 \\ B_2 \end{bmatrix}, \qquad C = \begin{bmatrix} C_1 & C_2 \end{bmatrix},$$

where

$$A_{11} = \begin{bmatrix} 0 & 1 \\ -\omega_1^2 & -c_{11} \end{bmatrix}, \quad B_1 = \begin{bmatrix} 0 & 0 \\ \cos\theta & \sin\theta \end{bmatrix}, \quad C_1 = \begin{bmatrix} 0 & \cos\theta \\ 0 & \sin\theta \end{bmatrix}, \quad \text{etc..}$$

If the off-diagonal damping term, c_{12}, is zero then the transfer function of (19) becomes (11) and θ is determined from the SVD of C_1B_1 or C_2B_2, either computation giving identical results. Under the circumstance when $c_{12} \neq 0$, the two modes do not decouple in the coordinates defined by the stiffness matrix eigenvectors. It is still possible to block-diagonalize A, however, with a more general state transformation. For example, suppose T is an invertible 4×4 matrix such that A is block-diagonalized, i.e.,

$$T^{-1}AT = \begin{bmatrix} \tilde{A}_{11} & 0_{2\times 2} \\ 0_{2\times 2} & \tilde{A}_{22} \end{bmatrix},$$

where $\tilde{A}_{11}$ and $\tilde{A}_{22}$ are the 2×2 blocks. The C matrix becomes CT and is partitioned into $\begin{bmatrix} \tilde{C}_1 & \tilde{C}_2 \end{bmatrix}$. The B matrix becomes $T^{-1}B$ and is partitioned into $\begin{bmatrix} \tilde{B}_1^T & \tilde{B}_2^T \end{bmatrix}^T$.

These block-diagonal coordinates are appealing because they are easy to compute from the *identified* model. Thus, it is natural to pose the following question: is it possible to estimate θ from the SVD of $\tilde{C}_1\tilde{B}_1$ or $\tilde{C}_2\tilde{B}_2$? We will answer this question in the affirmative by showing that the error in the θ estimate obtained from $\tilde{C}_1\tilde{B}_1$ or $\tilde{C}_2\tilde{B}_2$ is less than one degree. Analytical bounds are difficult to derive so we obtain numerical bounds from a parameter search that we now describe. First, ω_1 and ω_2 in (19) are fixed at the identified values of 534.5 Hz and 536.4 Hz, respectively. Then, the damping matrix parameters are chosen so that the matrix is positive semidefinite with eigenvalues between 0 and a specified constant $\delta \geq 0$. The eigenvectors of the damping matrix are free to be chosen. The state-space system specified with these parameters is then block-diagonlized with a state transformation and estimates of θ are obtained from $\tilde{C}_1\tilde{B}_1$ and $\tilde{C}_2\tilde{B}_2$.

The numerical search is carried out for a given bound δ and the damping matrix parameters are chosen to maximize the error between the estimates of θ determined from $\tilde{C}_1\tilde{B}_1$ and $\tilde{C}_2\tilde{B}_2$, and its true value. The search results are presented in Table 5.1. Without loss of generality, the true θ may be chosen as zero in the search, and the particular choice of block-diagonalizing state transformation is of no consequence because all block-diagonal forms of the A matrix in which the modes are decoupled are related via a block-diagonal similarity transform that leaves $\tilde{C}_1\tilde{B}_1$ and $\tilde{C}_2\tilde{B}_2$ invariant.

For the magnitudes of frequency separation and damping ratios identified here, a simple numerical study shows that

$$c_{ii} \approx 2\,\zeta_i\,\omega_i\,, \qquad i = 1, 2\,. \tag{20}$$

δ	0	1	2	4	8	16	32
$\Delta\theta$	0°	0.024°	0.10°	0.38°	1.5°	6.3°	45°

Table 1: Error in estimate of θ versus damping

The damping term c_{12} affects the eigenvalues and eigenvectors of the damping matrix but has almost no effect on the frequencies and damping ratios of the rocking modes. When the diagonal elements of the damping matrix are given by (20) with the identified values in (15) and the damping matrix is constrained to be positive semidefinite, its largest possible eigenvalue is

$$\delta = 2\,\zeta_1\,\omega_1 \; + 2\,\zeta_2\,\omega_2 \; = 3.2\,. \tag{21}$$

Hence, according to Table 5.1, the unknown damping term c_{12} should produce a $\Delta\theta$ of less than half a degree.

5.2 Description of the Rocking Modes

The method presented in this paper for identification of the stiffness axes assumes that, in each rocking mode, the cloverleaf and post rotate about a single fixed axis. In general, the rocking-mode motion is not so simple; however, the following discussion shows that, because of the light damping in the class of gyroscopes of interest here, the motion in each rocking mode closely approximates rotation about a single fixed stiffness axis.

The rocking modes are the eigen solutions to the system

$$\begin{bmatrix} \ddot{\psi}_1 \\ \ddot{\psi}_2 \end{bmatrix} + \begin{bmatrix} c_{11} & c_{12} \\ c_{12} & c_{22} \end{bmatrix} \begin{bmatrix} \dot{\psi}_1 \\ \dot{\psi}_2 \end{bmatrix} + \begin{bmatrix} \omega_1^2 & 0 \\ 0 & \omega_2^2 \end{bmatrix} \begin{bmatrix} \psi_1 \\ \psi_2 \end{bmatrix} = 0\,. \tag{22}$$

The eigen solutions can be written in the form

$$\begin{bmatrix} \psi_{1,i}(t) \\ \psi_{2,i}(t) \end{bmatrix} = \tag{23}$$
$$e^{-\zeta_i \bar{\omega}_i t} \left[u_{1,i}\, a_{1,i} \cos\left(\sqrt{1-\zeta_i^2}\, \tilde{\omega}_i t \right) + u_{2,i}\, a_{2,i} \cos\left(\sqrt{1-\zeta_i^2}\, \tilde{\omega}_i t + \phi_i \right) \right], \qquad i = 1, 2\,,$$

where, for each i, $u_{1,i}$ and $u_{2,i}$ are real, orthonormal, two-vectors, and $a_{1,i}$ and $a_{2,i}$ are nonnegative real amplitudes. For this discussion, $u_{1,1}$ is taken to be the real two-dimensional unit vector for which $a_{1,1}$ is maximum, and $u_{2,1}$ is taken to be the real two-dimensional unit vector for which $a_{2,1}$ is minimum. Also, $u_{1,2}$ is taken to be the real two-dimensional unit vector for which $a_{1,2}$ is minimum, and $u_{2,2}$ is taken to be the real two-dimensional unit vector for which $a_{2,2}$ is maximum. The angle between $u_{1,i}$ and the stiffness axis x_1 is denoted by ε_i.

$\Delta\omega$	$c_{12} =$	ε_1	ε_2	$a_{1,1}/a_{2,1}$	$a_{2,2}/a_{1,2}$
1.90 Hz	$\sqrt{c_{11}c_{22}}$	0.115°	0.163°	22.4	15.8
1.90 Hz	c_{22}	0.115°	0.115°	22.4	22.3
0.95 Hz	c_{22}	0.477°	0.468°	11.2	11.2

Table 2: Effects of c_{12} and $\Delta\omega = \omega_2 - \omega_1$ on rocking modes. For all cases, ω_1 and ζ_i are given by (15), and $c_{ii} = 2\,\zeta_i\,\omega_i$.

Because of the light damping in the gyros of interest here, the frequencies $\tilde{\omega}_i$ and $\sqrt{1-\zeta_i^2}\,\tilde{\omega}_i$ in (23) are essentially equal to ω_i. The identified rocking-mode damping ratios and frequencies given in (15).

For the identified frequency separation and range of damping, c_{12} has almost no effect on the eigenvalues of the system in (22). However, c_{12} can have a significant effect on the amplitudes $a_{1,i}$ and $a_{2,i}$. If $c_{12} = 0$, then $a_{2,1} = a_{1,2} = 0$; i.e., the motion in each rocking is rotation about a single fixed axis in the direction of one of the eigenvectors of the stiffness matrix. If $c_{12} \neq 0$, then in each rocking mode, the cloverleaf and post rotate about both stiffness axes, or equivalently, about axes in the directions of the unit vectors $u_{1,i}$ and $u_{2,i}$ in (23). However, for the damping ratios and frequencies identified, each rocking mode is dominated by rocking about a single stiffness axis, whatever the value of c_{12}. This conclusion follows from the an elementary numerical study summarized in Table 2.

Since the damping matrix must be positive semidefinite, the largest possible value for c_{12} is $\sqrt{c_{11}\,c_{22}}$. However, this value of c_{12} seems unrealistically large because it implies zero damping for rotation about some axis (since the damping matrix would have a zero eigenvalue.) With decreasing c_{12}, the ratios $a_{1,1}/a_{2,1}$ and $a_{2,2}/a_{1,2}$ increase and the angles ε_i decrease. Even $c_{12} = c_{22}$ probably is too large a value for c_{12} because, in this case, the damping matrix has eigenvalues of 2.7909 and 0.4053, meaning that the damping in the direction of greatest damping is almost seven times that in the direction of least damping.

As the frequency split decreases from the 1.9 Hz identified, the ratios of maximum amplitude to minimum amplitude decrease, until the frequency split becomes an order-of-magnitude smaller than that identified, and then the motion in each rocking mode begins to approach single-axis rocking about an axis in the direction of one of the damping-matrix eigenvalues. Because experimental identification of the frequencies should be quite accurate, as discussed in Section 4.1, the frequency split for the identified device should be very close the 1.9 Hz. Also, the results in Table 2 and for other damping ratios of similar magnitude show that, for the ranges of identified frequencies and damping ratios, the unidentified damping coefficient c_{12} has little effect on the directions of the rocking-mode axes, and does not cause the rocking-mode motion to deviate significantly from rocking about a single stiffness axes.

6 Conclusions

This paper addresses system identification and model development for the Jet Propulsion Laboratory microgyroscope. High-order, multi-input/multi-output linear models are required to capture important

characteristics of the gyro dynamics such as closely spaced modal frequencies. Lattice-filter-based algorithms are used to estimate the I/O models in this paper. The high-order models are truncated to a six-state model since the Hankel singular values of the balanced realization exhibit a decrease of several orders of magnitude beyond the first six states. Frequency response plots show that the three key modes corresponding to the sensor's two rocking modes and up-down mode are well-modeled with the six state approximation. The success of the lattice filter in identifying high-fidelity models of the microsensor in the current paper indicates the feasibility of real-time identification and calibration of such devices.

The error analysis motivates the importance of estimating the orientation of the principal axes of elasticity, or stiffness axes, with respect to the sensing pick-offs in addition to the frequency split between the rocking modes because both parameters contribute to quadrature and in-phase bias errors when estimating Ω. The frequency split and damping ratios are obtained from analyzing the eigenvalues of the identified model. The orientation of the stiffness axes, however, is also determined from further analysis since this information is not immediately available from the identified multi-input/output model and impossible to infer from the rocking mode frequency split alone. Our results show that the stiffness axes in the tested device are not aligned with the sense/drive electrode coordinate frame.

Acknowledgments: The authors thank Dr. Tony Tang, Chris Stell and Roman Gutierrez of the Jet Propulsion Laboratory, and Dorian Challoner of Hughes Space and Communications.

References:

1. Green, M., and Limebeer, D., 1995, *Linear Robust Control*, Prentice-Hall, New Jersey.

2. Jiang, S.-B., Gibson, J.S., and Hollkamp, J.J., 1992, "Identification of a Flexible Structure by a New Multichannel Lattice Filter," *Proc. of 1992 American Control Conference*, pp. 1681–1685.

3. Jiang, S.-B., and Gibson, J.S., 1995, "An unwindowed multichannel lattice filter with orthogonal channels," *IEEE Trans. on Signal Processing*, **43(12)**, pp. 2831-2842.

4. Lawrence, A., 1998, *Modern Inertial Technology: Navigation, Guidance, and Control*, Springer-Verlag, New York.

5. Lynch, D.D., 1995, "Vibratory Gyro Analysis by the Method of Averaging," *The 2nd Saint Petersburg International Conference on Gyroscopic Technology and Navigation*, Scientific Council of the Russian Academy of Sciences on the traffic control and navigation problems, Part I, pp. 26–34.

6. Lynch, D.D., 1998, "Coriolis Vibratory Gyros," *Symposium Gyro Technology*, Stuttgart, Vol. 1, pp. 1–14.

7. M'Closkey, R.T., Vakakis, A.F., and Gutierrez, R., 2000, "Mode Localization Induced by a Nonlinear Control Loop," *Nonlinear Dynamics* (to appear).

8. Morrow, C.T., 1955, "Zero Signals in the Sperry Tuning Fork Gyrotron," *J. Accoustical Society of America*, Vol. 27, No. 3, pp. 581–585.

9. Newton, G.C., 1963, "Theory and Practice in Vibratory Rate Gyros," *Control Engineering*, pp. 95–99.

10. Tang, T.K., Gutierrez, R.C., Wilcox, J.Z., Stell, C., Voperian, V., Calvet, R., Li, W., Charkaborty, I., Bartman, R., and Kaiser, W.J., 1996a, "Silicon Bulk Micromachined Vibratory Gyroscope." *Solid-State Sensor and Actuator Workshop*, Hilton Head, SC, pp. 288–293.

11. Tang, T.K., Gutierrez, R.C., Wilcox, J.Z., Stell, C., Vorperian, V., Dickerson, M., Goldstein, B., Savino, J.L., Li, W.J., and Calvet,R., 1996b, "Silicon bulk micromachined vibratory gyroscope for microspacecraft." in *Proc. of the SPIE*, Denver, CO, Vol. 2810, pp. 101-115.

12. Tang, T.K., Gutierrez, R.C., Stell, C.B., Vorperian, V., Arakaki, G.A., Rice, J.T., Li, W.J., Chakraborty, I., Shcheglov, K., Wilcox, J.Z., and Kaiser, W.J., 1997, "A packaged silicon MEMS vibratory gyroscope for microspacecraft," *Proc. IEEE*, The Tenth Annual International Workshop on Micro Electro Mechanical Systems, Nagoya, Japan, pp. 500-505.

13. Yazdi, N., Ayazi, F., and Najafi, K., 1998, "Micromachined Inertial Sensors," *Proc. IEEE*, Vol. 86, No. 8, pp. 1640–1659.

14. Zhbanov, Yu.K., Zhuravlev, V.F., 1998, "On the balancing of a hemispherical resonator gyro," *Mechanics of Solids*, Vol. 33, No. 4, pp. 2-13 (translated).

15. Zhou, K., Doyle, J., and Glover, K., 1996, *Robust and Optimal Control*, Prentice Hall, New Jersey.

List of Figures:

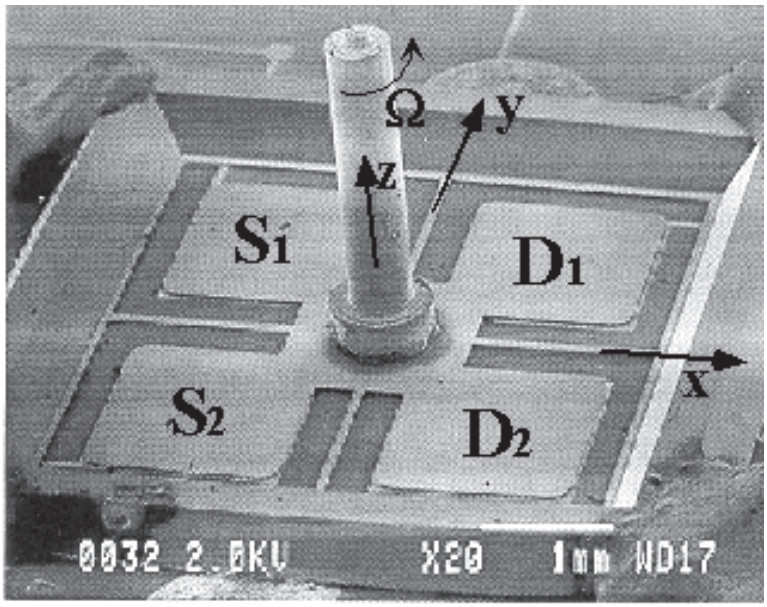

Figure 1: JPL microgyro with sense and actuator electrodes labeled (picture courtesy of T. Tang)

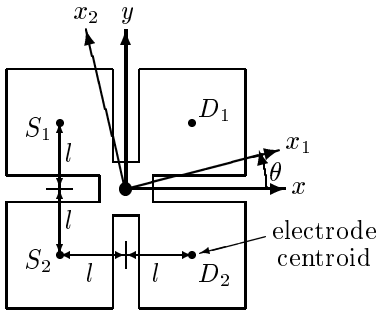

Figure 2: Top view of cloverleaf structure with principal axes of stiffness matrix (x_1–x_2 frame) at orientation angle θ with respect to the measurement/actuation coordinates (x–y frame).

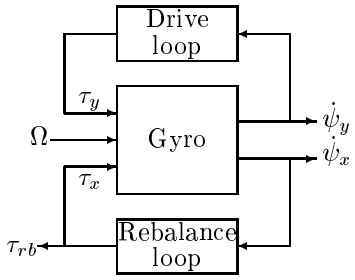

Figure 3: Sense and drive axis control loops.

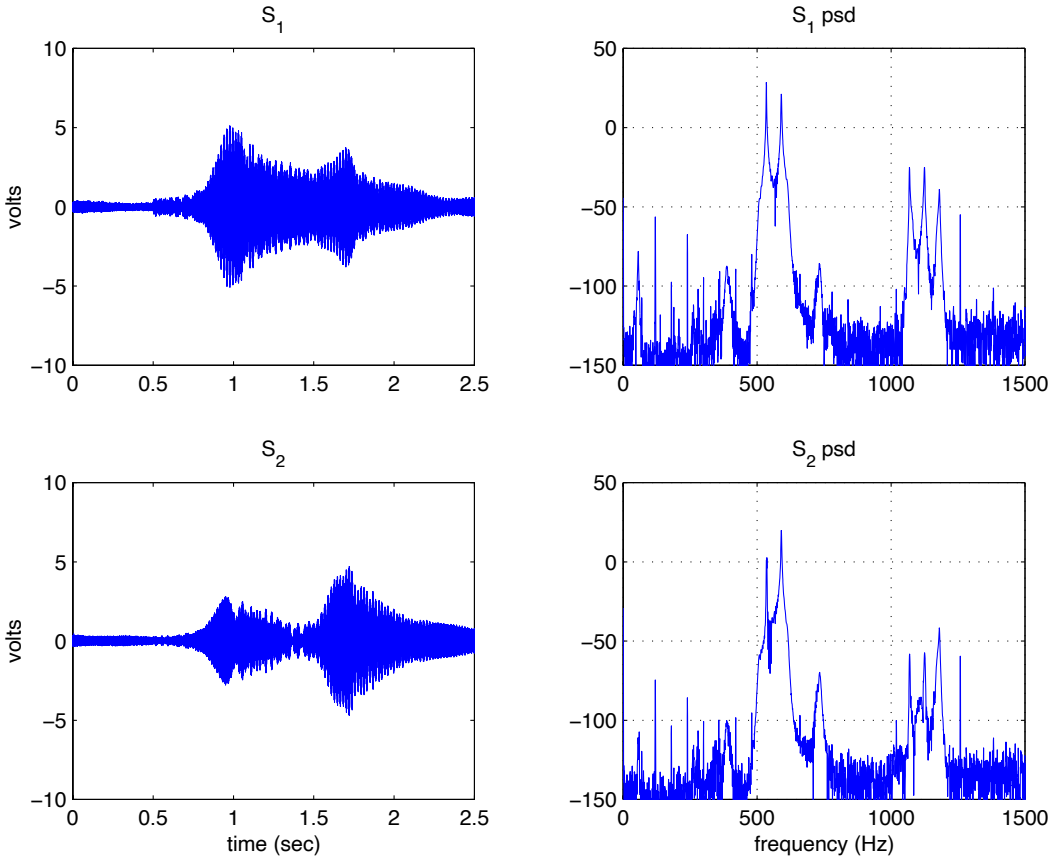

Figure 4: Output sequences and power spectral densities (in dB).

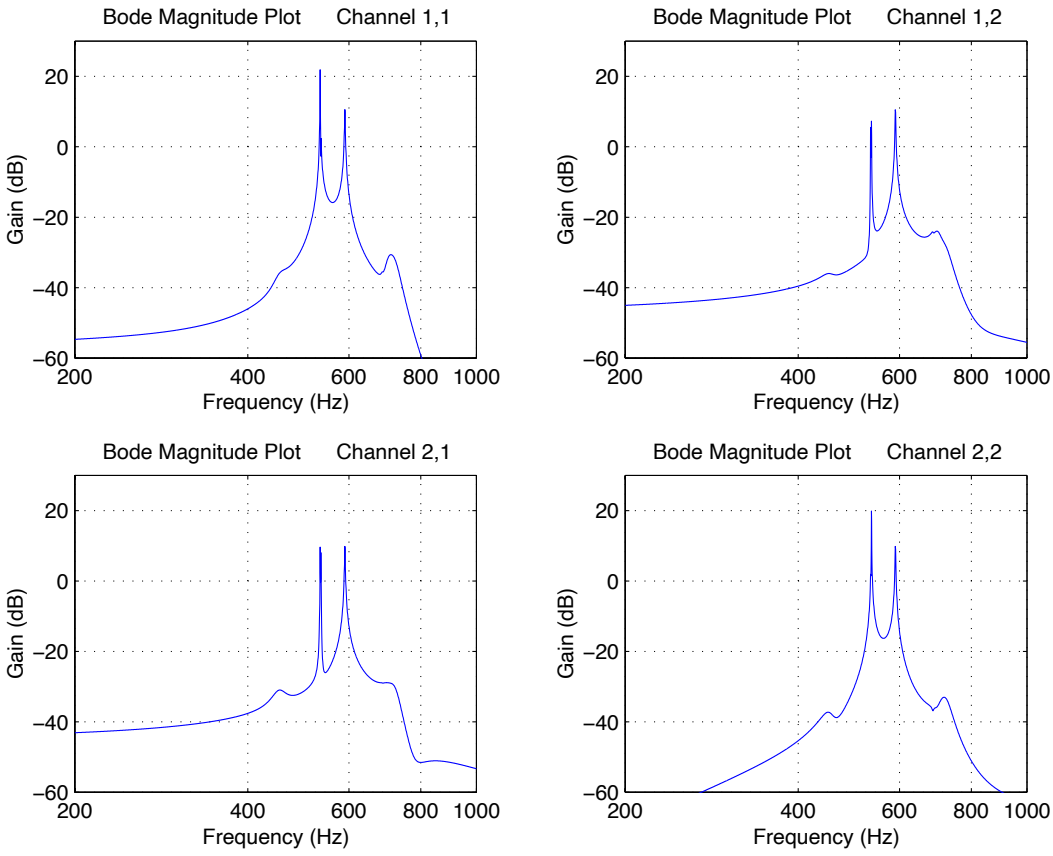

Figure 5: Identified 40th-order MIMO model.

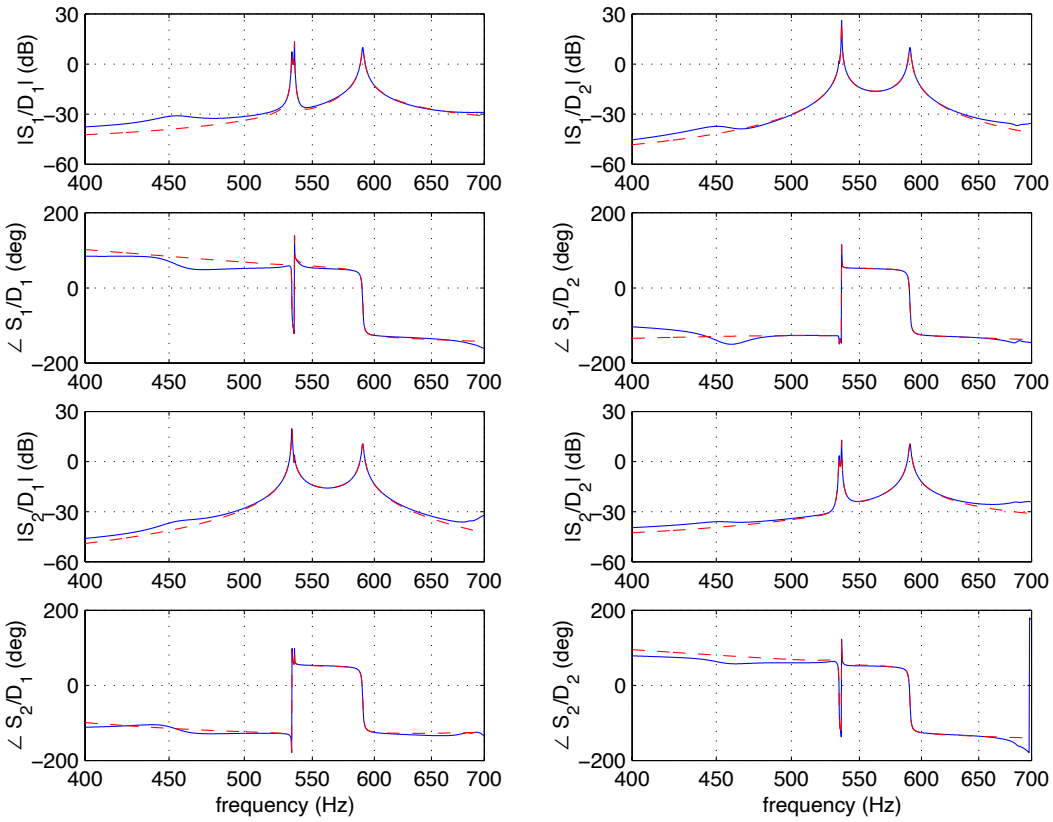

Figure 6: Comparison of 40th-order model (solid) and 6 state balanced truncation (dash).